

Ultralong-Range Periodic Alignment and Structural Coloration of Titanate and Titanoniobate Nanosheets in Aqueous Dispersions

Takayuki Kikuchi, Yasuo Ebina, Nobuyuki Sakai, Yoshiyuki Sugahara, Takayoshi Sasaki,* and Renzhi Ma*



Cite This: JACS Au 2025, 5, 5207–5216



Read Online

ACCESS |

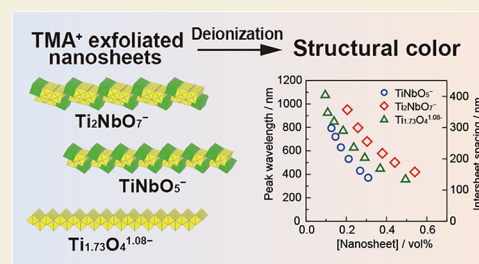
Metrics & More

Article Recommendations

Supporting Information

ABSTRACT: Structural coloration has been reported for many types of two-dimensional (2D) materials, including metal oxide nanosheets. In particular, metal oxide nanosheets feature a wealth of composition and structure, but their impact on structural color has not been explored. In the current study, we report the structural coloration observed for aqueous suspensions of three types of transition metal oxide nanosheets ($\text{Ti}_{1.73}\text{O}_4^{1.08-}$, TiNbO_5^- , and $\text{Ti}_2\text{NbO}_7^-$) obtained via the exfoliation of precursory layered compounds with tetramethylammonium hydroxide (TMAOH). It was revealed that a minute amount of TMA^+ was retained even after deionization via repeated centrifugation, acting as counteranions to the negatively charged nanosheets. These residual TMA^+ ions contributed to stabilizing the dispersion of nanosheets under low-ionic-strength conditions, while the intersheet spacing was expanded to a magnitude comparable to the wavelength of the visible-light range, resulting in structural coloration. The wavelength of structural colors was dependent not only on nanosheet concentration but also on the type of nanosheets, correlating with the charge (ζ -potential) and thickness of the nanosheets, as well as the amount of TMA^+ dissociated from the nanosheet surfaces. Specifically, TiNbO_5^- was featured with the highest amount of TMA^+ in the solution, which screened the negative charge of the nanosheets and resulted in the smallest intersheet spacing. On the other hand, when the dissociated amount of TMA^+ was diminished, $\text{Ti}_2\text{NbO}_7^-$, with a larger thickness, yielded a larger intersheet spacing than that of $\text{Ti}_{1.73}\text{O}_4^{1.08-}$. These findings provide a valuable clue to the rational control of structural colors derived from nanosheets with different compositions and structures for a wide range of applications.

KEYWORDS: structural coloration, liquid crystallinity, metal oxide nanosheets, surface charge, ionic strength



INTRODUCTION

In 1949, Onsager proposed that materials with anisotropic shapes orderly arrange themselves in a solution to form liquid crystals to minimize the entropy in the system.¹ For instance, if colloidal particles possess a large two-dimensional (2D) anisotropy, they tend to align cofacially and form nematic or lamellar liquid crystal phases. A study on the dispersion behavior of anisotropic particles, including 2D materials, is of great interest, as it could lead to rational control and improvement of the mechanical, thermal, optical, and electrical properties of colloidal/liquid crystalline materials.

On the other hand, it has been established that soft chemical processes could be applied to produce 2D materials with high aspect ratios in colloidal suspensions, so-called nanosheets. In 1998, our group reported the synthesis of titanate ($\text{Ti}_{0.91}\text{O}_2^{0.36-}$) nanosheets with a thickness of 1 nm.^{2,3} In this soft chemical procedure, gigantic osmotic swelling of layered titanates is induced by the intercalation of a bulky organic amine, and subsequent exfoliation into monolayer nanosheets is attained by applying an external force. Such a synthetic method has been applied to various compounds to obtain a range of nanosheets with various compositions,^{4,5} including

titanoniobate nanosheets.^{6–8} The dispersion behavior of the 2D nanosheets with anisotropic shapes was then studied. Nakato and Miyamoto reported that several kinds of oxide nanosheet suspensions exhibited liquid crystalline behavior.^{9–11} Typical periodic intersheet spacing of such liquid crystals was several tens of nanometers. Recently, Sano et al. reported the observation of structural color from titanate nanosheet suspensions with reduced ionic strength.¹² Titanate nanosheets were found to align regularly at an ultralong intersheet distance of up to 675 nm, and the suspensions were able to reflect light from the UV to near-infrared (IR) range, depending on the nanosheet concentration. Surprisingly, the liquid crystal forms a centimeter-scale monodomain upon application of a strong magnetic field, exhibiting uniform and vivid structural color. Currently, liquid crystalline property and

Received: September 3, 2025

Revised: September 26, 2025

Accepted: September 29, 2025

Published: October 10, 2025



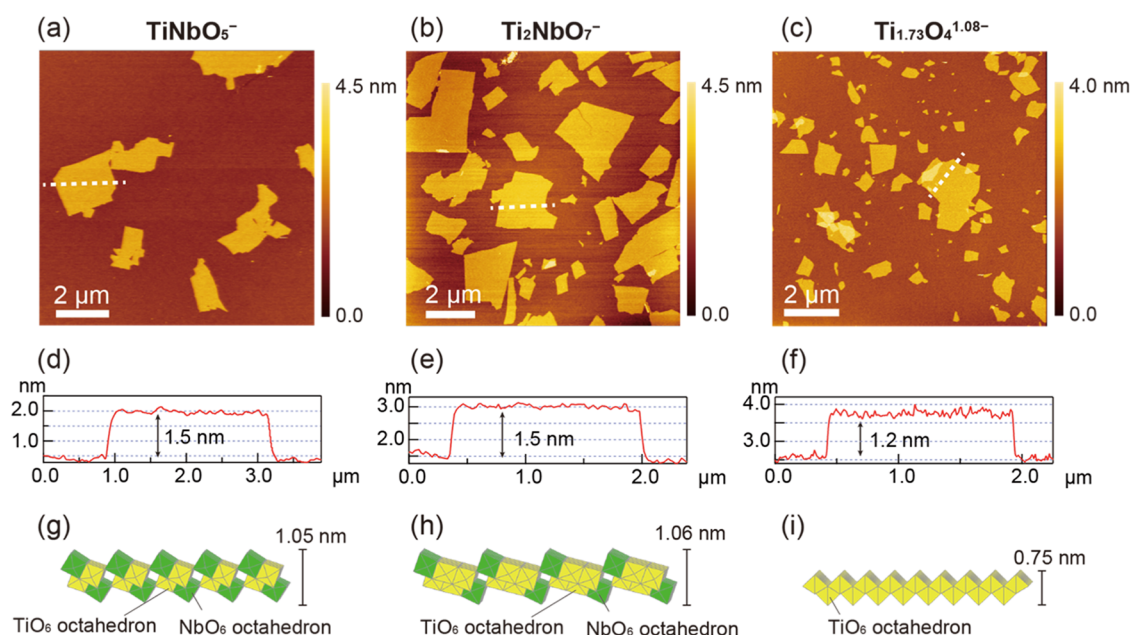


Figure 1. Typical AFM images of three types of nanosheets measured under ambient conditions: (a) TiNbO_5^- , (b) $\text{Ti}_2\text{NbO}_7^-$, and (c) $\text{Ti}_{1.73}\text{O}_4^{1.08-}$. The corresponding height profiles (d–f) and structures of the nanosheets (g–i).

structural coloration have been confirmed for various 2D materials, e.g., graphene oxide,^{13,14} phosphate,^{15–20} hexaniobate,²¹ fluorinated clay,^{22,23} and layered perovskites.²⁴ However, any other nanosheet dispersion that can reflect up to near-infrared light comparable to that of titanate nanosheets has not been reported except for a fluorinated clay.²² Such an unusual ultralong-range periodic alignment might be deeply related to the structural feature and resultant dispersion behavior of the nanosheets, but a comparative study of different types of nanosheets is not available.

In this study, three types of transition metal oxide nanosheets, titanate ($\text{Ti}_{1.73}\text{O}_4^{1.08-}$) and titanoniobate (TiNbO_5^- and $\text{Ti}_2\text{NbO}_7^-$) nanosheets, were explored in terms of their structural colors. These nanosheets were selected as ideal model systems for comparative studies of structural color based on several important criteria, including high refractive index, transparency in the visible-light region, strong negative surface charge that enables stable dispersion, highly tunable composition, and ease of synthesis (synthetic accessibility). The nanosheets were derived from $\text{K}_{0.8}\text{Ti}_{1.73}\text{Li}_{0.27}\text{O}_4$, KTiNbO_5 , and $\text{CsTi}_2\text{NbO}_7$ via acid exchange and subsequent exfoliation with the tetramethylammonium hydroxide (TMAOH) solution, a common delaminating agent. The structural color was then observed after repeated sedimentation of nanosheets by centrifugation and redispersion with pure water. Structural colorations were examined by measuring the ion conductivity, pH, and ζ -potential values, as well as nuclear magnetic resonance (NMR) and UV–vis reflectance spectroscopy. Upon repeated deionization, a minute amount of dissociated TMA^+ was retained, which acts as counteranions of the nanosheets, allowing them to maintain their dispersed states. Furthermore, the Debye screening length increased with the removal of ions in the solution, resulting in an expansion of the intersheet spacing to a degree comparable to that in the visible-light wavelength range. This highly expanded lamellar structure induces the interference of visible light, leading to the evolution of structural colors. The wavelength of the structural color was

influenced not only by the concentration of the nanosheets but also by their composition, which is correlated to their charge (ζ -potential) and thickness. At similar concentrations, the intersheet spacing increased in the order of TiNbO_5^- (180 nm, 0.31 vol %), $\text{Ti}_{1.73}\text{O}_4^{1.08-}$ (203 nm, 0.29 vol %), and $\text{Ti}_2\text{NbO}_7^-$ (256 nm, 0.30 vol %). These findings thus offer valuable insights into the rational control of structural colors derived from 2D nanosheets with various compositions and structures, holding great potential for applications in reflective displays²⁵ and chemical sensors.^{12,26–29}

RESULTS AND DISCUSSION

Figure 1 shows atomic force microscopy (AFM) images and structure models of three types of metal oxide nanosheets, TiNbO_5^- , $\text{Ti}_2\text{NbO}_7^-$, and $\text{Ti}_{1.73}\text{O}_4^{1.08-}$. All nanosheets exhibit uniform molecular thicknesses of 1.5 nm for TiNbO_5^- and $\text{Ti}_2\text{NbO}_7^-$ and 1.2 nm for $\text{Ti}_{1.73}\text{O}_4^{1.08-}$. The measured thickness can be understood in terms of the sum of the crystallographic thickness of the host layer (TiNbO_5^- : 1.05 nm, $\text{Ti}_2\text{NbO}_7^-$: 1.06 nm, $\text{Ti}_{1.73}\text{O}_4^{1.08-}$: 0.75 nm) and the size of surface-adsorbed species such as water molecules and/or TMA^+ ions. This feature has been observed for a range of nanosheets and taken as evidence for the formation of single-layer nanosheets.^{3,30} AFM measurements were also performed after the adsorbed molecules were removed by UV irradiation and vacuum heating. As depicted in Figure S1 (Supporting Information), the thicknesses were reduced to 1.1 nm for TiNbO_5^- and $\text{Ti}_2\text{NbO}_7^-$ and 0.8 nm for $\text{Ti}_{1.73}\text{O}_4^{1.08-}$. The values measured under high vacuum are in good agreement with the respective crystallographic thicknesses, reinforcing the interpretation that the increased thickness under ambient conditions originates from the presence of such surface species. AFM images over a wide area were collected and used to analyze the lateral size distribution of the nanosheets (Figure S2). The obtained histograms show that the average size of the nanosheets falls in a range of several hundred nanometers to a few micrometers, which is thousands of times larger than their thickness, yielding a high aspect ratio of approximately 1000. It

is noteworthy that the as-exfoliated $\text{Ti}_{1.73}\text{O}_4^{1.08-}$ nanosheets exhibit a much larger size (5–10 μm) than the other two types of nanosheets, which can be reduced by ultrasonic fragmentation (Figure S3). The sample after ultrasonic fragmentation for 2 h displays a size distribution comparable to those of TiNbO_5^- and $\text{Ti}_2\text{NbO}_7^-$ (Figure S2). To minimize the possible size effect on the structural coloration behavior, the fragmented $\text{Ti}_{1.73}\text{O}_4^{1.08-}$ nanosheets were used in the following procedures.

TMA⁺ ions in the suspension were removed by settling out the nanosheets upon centrifugation and redispersion with water. To remove the electrolyte as much as possible, this process was repeated more than 10 times. The concentration of the nanosheets was readily adjusted in the final step by controlling the amount of pure water added for redispersion. The deionized suspension was injected into a homemade thin cell composed of quartz glass and a spacer to observe the structural color (Figure S4). The lamellar domains tended to align parallel to the cell face, as the nanosheets exhibited a cofacial orientation under the shear force generated by the injection into the cell. As shown in Figure 2, a vivid structural color appeared. It is obvious that these structural colors are derived from the Bragg reflection of the nanosheets separated by a long distance comparable to the visible-light wavelength range. The change in structural color and the corresponding shift in the peak of reflectance spectra were dependent on the concentration of nanosheets. In general, a deep blue color was observed at a high concentration of nanosheets. As the concentration decreased, the color became weaker due to a deteriorated orientation order of nanosheets, and the wavelength also red-shifted. In a dilute suspension, in which the intersheet spacing is sufficiently wide, multiple reflection peaks caused by higher-order Bragg reflections, such as second- and third-order reflections, may be observed in the visible region. For example, in the $\text{Ti}_2\text{NbO}_7^-$ dispersion with a volume fraction of 0.21 vol %, the first-order peak was located in the infrared region at the wavelength of 951 nm, while the second-order peak fell in the visible region at 476 nm, yielding a light blue color. As dilution progressed further, the orientation order of the nanosheets gradually deteriorated, and the intensity of the reflection peak became weaker, eventually causing the disappearance of the structural color.

Figure 3 shows the relationship between the structural color and the nanosheet volume fraction in deionized suspensions. As schematically illustrated in Figure 3a, decreasing the nanosheet concentration expands the intersheet spacing, resulting in a red shift of the first-order Bragg reflection. The intersheet spacing (d) is calculated from the peak-top wavelength (λ) using Bragg's equation ($m\lambda = 2n_{\text{av}}d \sin \theta$, where m represents diffraction order and n_{av} represents the averaged refractive index (1.33) of the suspension).¹² As shown in Figure 3b, it is obvious that the intersheet spacings of the desalinated nanosheet suspensions vary for each type of nanosheet. For example, titanoniobate nanosheets with different compositions, TiNbO_5^- and $\text{Ti}_2\text{NbO}_7^-$, exhibit significantly different interlayer spacings even at the same volume fraction. Specifically, the periodic spacing of TiNbO_5^- and $\text{Ti}_2\text{NbO}_7^-$ suspensions containing the same total volume of nanosheets (0.21 vol %) deviates significantly over 150 nm. As TiNbO_5^- yields the smallest intersheet spacing, the concentration range in which structural colors can be observed is also the narrowest.

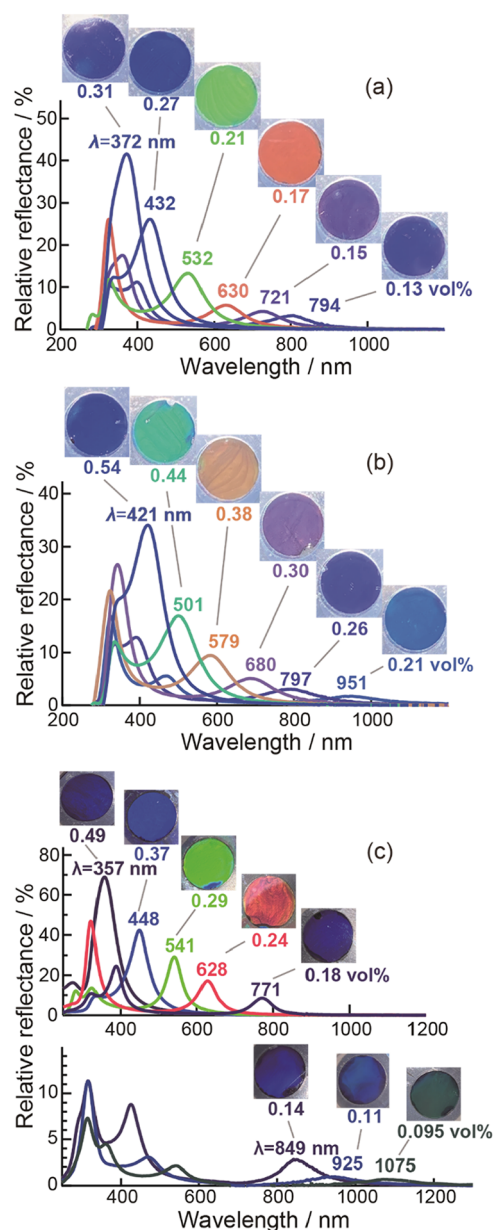


Figure 2. Appearance of structural colors observed from nanosheet suspensions and the corresponding reflectance spectra with different volume fractions (vol %) of nanosheets: (a) TiNbO_5^- , (b) $\text{Ti}_2\text{NbO}_7^-$, and (c) $\text{Ti}_{1.73}\text{O}_4^{1.08-}$. The peak wavelengths are labeled.

According to Onsager's theory,¹ when 2D materials form liquid crystals, the degree of orientation varies with their concentration and aspect ratio. It has been experimentally confirmed that at a high concentration, nanosheets tend to align uniaxially in the suspension. As the concentration decreases, the nanosheets gradually lose the orientation order.³¹ It is assumed that these nanosheets are fully oriented and packed into an ideal lamellar structure, as schematically illustrated in Figure 4a. The intersheet spacing can be estimated using the following equation.

$$d = t / \phi_{\text{NS}} \quad (1)$$

where t is the thickness of the nanosheets and ϕ_{NS} is the volume fraction of the nanosheets.

Equation 1 indicates that the intersheet spacing is proportional to the inverse of the volume fraction. At the same

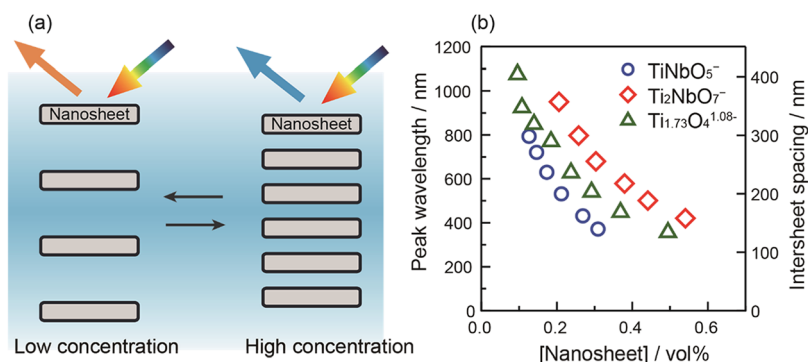


Figure 3. (a) Schematic illustration of the concentration-dependent change in intersheet spacing and the corresponding structural colors from the nanosheet suspensions. (b) First-order peak wavelengths of structural colors and the corresponding intersheet spacings observed from various deionized nanosheet dispersions. As the nanosheet volume fraction decreases, the intersheet spacing increases, resulting in a red shift of the Bragg reflection.

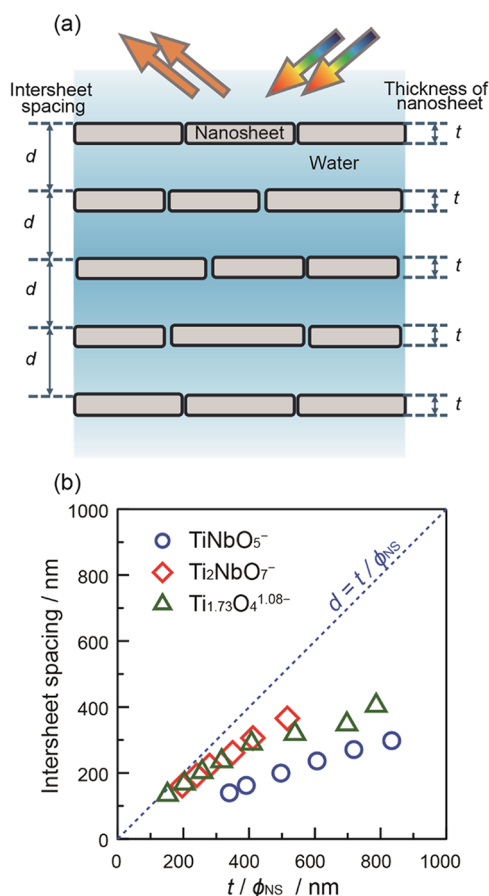


Figure 4. (a) Ideal lamellar structure model composed of aligned and packed nanosheets in a deionized suspension. The volume fraction of nanosheets (ϕ_{NS}) can be estimated by intersheet spacing (d) and nanosheet thickness (t), $\phi_{\text{NS}} = t/d$. (b) Dependence of measured intersheet spacing on the nanosheet thickness divided by the volume fraction. The dotted line represents a calculated intersheet spacing in the ideal lamellar model, $d = t/\phi_{\text{NS}}$.

nanosheet volume fraction, the intersheet spacing is proportional to the nanosheet thickness. As shown in Figure 4b, all measured intersheet spacings deviate downward from a dotted line representing the ideal lamellar model, as defined by eq 1. The deviation might be caused by the orientation disorder of the nanosheets or the insufficient development of lamellar domains. On the other hand, Sano et al. reported intersheet

spacings in good agreement with eq 1 when $\text{Ti}_{1.73}\text{O}_4^{1.08-}$ nanosheets with a large average size were aligned by a strong magnetic field.¹² It implies that both size distribution and orientation enhancement of nanosheets may affect the intersheet spacing, which awaits further study. Integration of additional structural characterization methods, such as polarized optical microscopy (POM) and 2D-small angle X-ray scattering (SAXS) could provide valuable complementary insights into nanosheet alignment and lamellar ordering, which is currently being explored. As aforementioned, to minimize the size effect, all three types of nanosheets with comparable size distribution were employed in the current study. The plots of $\text{Ti}_2\text{NbO}_7^-$ and $\text{Ti}_{1.73}\text{O}_4^{1.08-}$ almost overlap with each other at the intersheet spacing between 160 and 300 nm. This suggests that $\text{Ti}_2\text{NbO}_7^-$ and $\text{Ti}_{1.73}\text{O}_4^{1.08-}$ nanosheets behave almost identically despite their different thicknesses ($\text{Ti}_{1.73}\text{O}_4^{1.08-}$: 0.75 nm, $\text{Ti}_2\text{NbO}_7^-$: 1.06 nm). On the other hand, although TiNbO_5^- and $\text{Ti}_2\text{NbO}_7^-$ nanosheets possess the same thickness, their plots deviate significantly. The smaller intersheet spacing of TiNbO_5^- may be due to insufficient electrostatic repulsion. To explore this difference, the ionic strength of the nanosheet suspensions was further evaluated and compared.

Figure 5 shows the changes in pH and ionic conductivity during the deionization process. The volume fraction of nanosheets was unified at 0.04 vol %. In Figure 5a, the obtained pH values of the as-prepared nanosheet suspensions indicated strong basicity, which gradually decreased toward neutral as the hydroxide ions in the system were removed by repeating deionization. At the same time, some TMA^+ ions also tend to detach from the nanosheet surface as the ionic strength decreases. However, a strong electrostatic attraction between TMA^+ ions and the negatively charged nanosheets helps to retain a minimal amount of adsorbed TMA^+ ions, even after repeated deionization. The residual TMA^+ ions are essential in maintaining colloidal stability and suppressing the aggregation of nanosheets. After 10 cycles of deionization, all of the suspensions changed to weak base, with the pH value 9.0 for TiNbO_5^- , 8.0 for $\text{Ti}_2\text{NbO}_7^-$, and 8.5 for $\text{Ti}_{1.73}\text{O}_4^{1.08-}$. Figure 5b shows the change in ionic conductivity. The nanosheet suspension contains mainly TMA^+ ions, which are the counterions to the negatively charged nanosheets, and residual hydroxide ions, as can be seen from the pH measurements. The ionic conductivity can thus be estimated from the mobility and number density of the nanosheets and

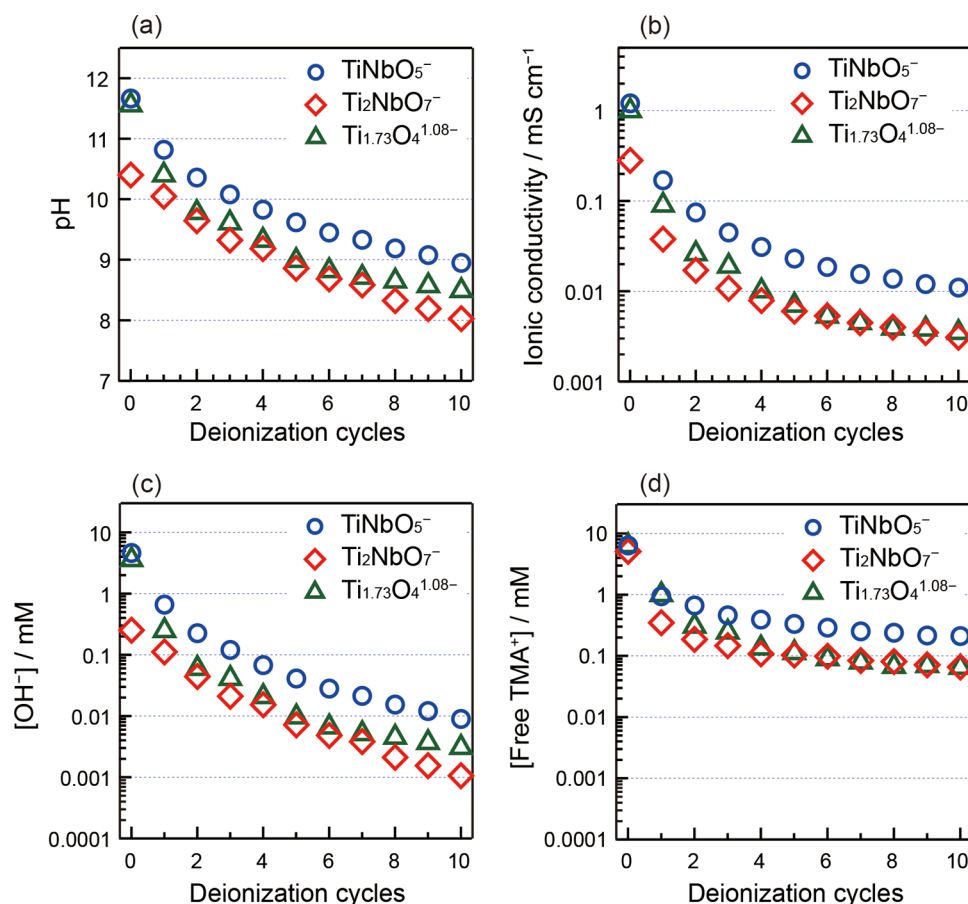


Figure 5. Changes in (a) pH and (b) ionic conductivity as functions of the number of deionization cycles. Suspensions of the same volume fraction of nanosheets, 0.04 vol %, were used. Each data point represents an averaged value of 4 samples. Variations in (c) hydroxide ion (OH^-) and (d) TMA^+ concentrations were estimated from the pH and ionic conductivity measurements.

the dissociated ions (TMA^+ , OH^-) by the following equation:³²

$$\sigma = n_p Z_{\text{eff}} e (\mu_p + \mu_H) + \sum_i n_i e \mu_i \quad (2)$$

where σ is the ionic conductivity of the suspension; n_p and n_i are the number density of nanosheets and ions, respectively; Z_{eff} is the effective charge of nanosheets; e is the elementary charge; and μ_p , μ_H , and μ_i represent the mobility of nanosheets, adsorbed counterions, and dissociated ions, respectively.

The mobility values of TMA^+ and OH^- are reported to be 4.66×10^{-4} and $20.64 \times 10^{-4} \text{ cm}^2 \text{ V}^{-1} \text{ s}^{-1}$, respectively.³³ On the other hand, the mobility of the nanosheets obtained from the ζ -potential measurements was in the range of 3.8×10^{-4} to $6.2 \times 10^{-4} \text{ cm}^2 \text{ V}^{-1} \text{ s}^{-1}$, comparable to those of the ions. As the number density of $\text{Ti}_{1.73}\text{O}_4^{1.08-}$ nanosheets with an average lateral size of $1 \mu\text{m}$ at 0.04 vol % is estimated to be $6.8 \times 10^{17} \text{ m}^{-3}$, which is sufficiently small compared to $6.0 \times 10^{20} \text{ m}^{-3}$ of dissociated ions at $1 \mu\text{M}$, the contribution of the nanosheets to ion conductivity is negligible. Number density of dissociated TMA^+ ions (n_{TMA^+}) can therefore be calculated as follows.

$$n_{\text{TMA}^+} = \frac{\sigma - e \mu_{\text{OH}^-} n_{\text{OH}^-}}{e \mu_{\text{TMA}^+}} \quad (3)$$

In eq 3, n_{OH^-} can be obtained from the pH value. The variation of the OH^- and TMA^+ concentrations is plotted in Figure 5c,d. It can be seen that, after repeated deionization, the

concentrations of OH^- and TMA^+ in the deionized TiNbO_5^- suspension are higher than those of $\text{Ti}_{1.73}\text{O}_4^{1.08-}$ and $\text{Ti}_2\text{NbO}_7^-$.

The ionic strength (I) of the deionized nanosheet suspension can be determined from the concentrations of the dissociated TMA^+ and OH^- by following eq 4:

$$I = \frac{1}{2} \sum C_i Z_i^2 = \frac{1}{2} ([\text{TMA}^+] + [\text{OH}^-]) \quad (4)$$

where C represents the concentration of each ion and Z denotes the valence.

The calculated values of the three types of nanosheet suspensions are summarized in Table 1. It clearly shows that the ionic strength of TiNbO_5^- , 0.11 mM, is significantly larger than that of $\text{Ti}_2\text{NbO}_7^-$ (0.033 mM) and $\text{Ti}_{1.73}\text{O}_4^{1.08-}$ (0.034 mM).

According to the Derjaguin–Landau–Verwey–Overbeek (DLVO) theory,^{12,34} a diffuse electric double layer may form in the vicinity of the charged nanosheets. When the nanosheets approach each other, the electric double layers start to overlap, causing repulsive forces and preventing aggregation. The thickness of this diffuse electric double layer is known as the inverse of the Debye screening length κ , which is proportional to the square root of ionic strength according to the following equation:

$$\kappa \propto \sqrt{\frac{I}{\epsilon T}} \quad (5)$$

Table 1. Ionic Environments of Deionized Nanosheet Dispersions with a Volume Fraction of 0.04 vol %^a

| | TiNbO ₅ [−] | Ti ₂ NbO ₇ [−] | Ti _{1.73} O ₄ ^{1.08−} |
|--|---------------------------------|---|--|
| nanosheet (NS) concentration (mM) | 5.7 | 3.5 | 7.4 |
| dissociated TMA ⁺ (mM) | 0.21 | 0.065 | 0.064 |
| [OH [−]] (mM) | 0.0090 | 0.0011 | 0.0031 |
| ionic strength (mM) | 0.11 | 0.033 | 0.034 |
| ζ-potential (mV) | −46.2 | −72.2 | −74.5 |
| adsorbed TMA ⁺ [TMA _{ad} ⁺] (mM) | 2.8 | 1.1 | 1.7 |
| [TMA _{ad} ⁺]/[NS] | 0.49 | 0.31 | 0.23 |
| replacement rate of exchangeable protons | 49% | 32% | 21% |
| percentage of exchangeable protons in protonic oxides | 44.1% | 37.5% | 24.5% |
| charge density of nanosheets (e nm ^{−2}) | 8.2 | 5.7 | 9.5 |

^a[TMA_{ad}⁺]/[NS] represents the molar ratio of adsorbed TMA⁺ to nanosheets.

where ϵ is the dielectric constant of the suspension and T is the temperature.

In an ideal lamellar model, the intersheet spacing may be roughly estimated by the Debye screening length according to eq 6.³⁵

$$d \cong \frac{4}{\kappa} \quad (6)$$

From eqs 5 and 6, a smaller ionic strength broadens the diffuse electric double layer, resulting in the formation of a larger intersheet spacing. This tendency is consistent with the experimental results that the suspensions of Ti₂NbO₇[−] and Ti_{1.73}O₄^{1.08−} exhibit an intersheet spacing larger than that of TiNbO₅[−]. In addition, ζ-potential is another parameter representing the magnitude of electrostatic repulsion or attraction between the nanosheets, which is important in understanding the electrochemical equilibrium of the nanosheet dispersions. Again, larger ζ-potential values of Ti₂NbO₇[−] and Ti_{1.73}O₄^{1.08−} nanosheets correspond well to the larger intersheet spacing than that of TiNbO₅[−].

As shown in Table 1, the total amount of TMA⁺ quantified by NMR is significantly larger than that of the dissociated TMA⁺ ions estimated by the ionic conductivity. The results indicate that approximately 1/5 to 1/2 of the exchangeable protons in HTiNbO₅, HTi₂NbO₇, and H_{1.08}Ti_{1.73}O₄ are replaced by TMA⁺ ions, which are mainly adsorbed on the negatively charged nanosheet surface. Due to strong electrostatic interactions between TMA⁺ ions and the adsorption sites, the adsorbed TMA⁺ are retained even after repeated deionization. Furthermore, the results are also consistent with the number and trend of exchangeable proton sites contained in the corresponding layered protonic oxides as evaluated by cation-exchange with ammonium acetate (Table S1). Therefore, the adsorption amount of TMA⁺ ions may reflect the inherent solid acidity of the nanosheets, which originates from the Brønsted acid sites associated with their metal–oxygen

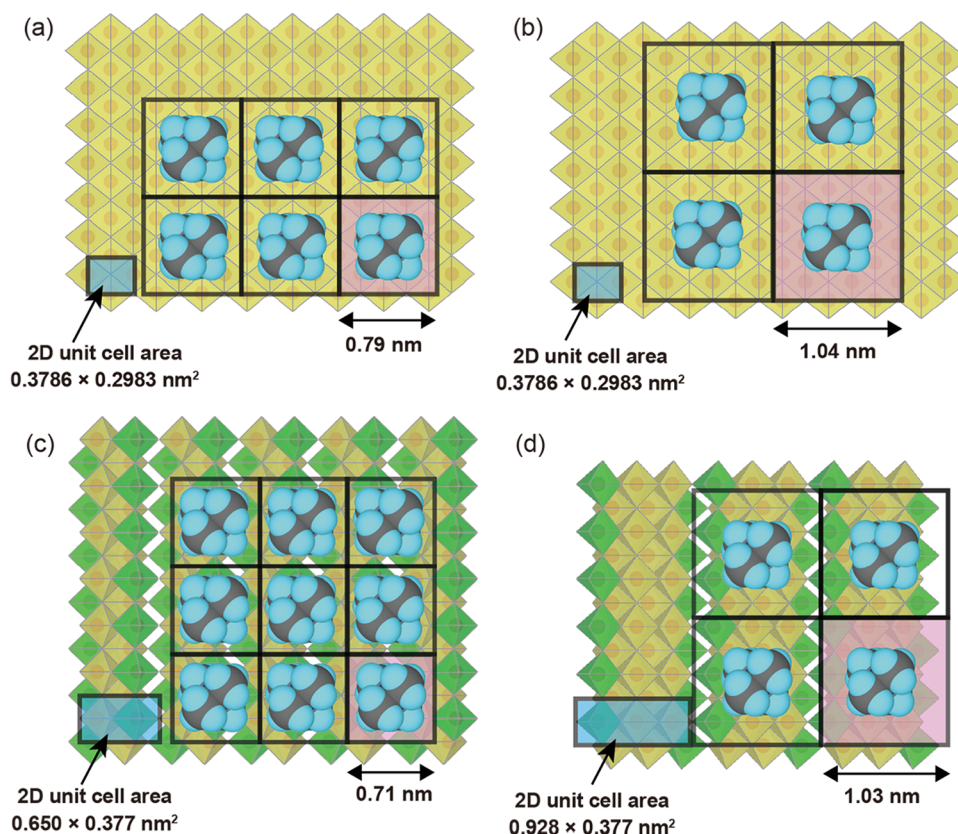


Figure 6. Schematic illustrations of adsorbed TMA⁺ ions on the host layer of (a) Ti_{1.73}O₄^{1.08−} swollen crystal³⁷ and on the surfaces of (b) Ti_{1.73}O₄^{1.08−}, (c) TiNbO₅[−], and (d) Ti₂NbO₇[−] nanosheets after repeated deionization. The pink area in each panel indicates the projected area per one TMA⁺ ion based on the experimentally determined adsorption density. Panel a was adapted with permission from ref 37, Copyright 2024 Wiley-VCH. All crystal structures were visualized using VESTA.³⁸

framework and local coordination structure.^{7,36} In the deionized suspensions, only a minute amount of TMA⁺ ions dissociates as free ions to form an electrical double layer. Such a low-ionic-strength condition enables the expansion of the intersheet spacing to a degree comparable to the visible wavelength range, resulting in structural coloration.

In the previous study on the swelling/delamination reaction of layered metal oxides with quaternary ammonium ions, a replacement rate of 34% of exchangeable protons in H_{1.08}Ti_{1.73}O₄ was found at the equivalent dose of TMA⁺ ions,³⁷ which is higher than the corresponding value of 21% as indicated in Table 1. To visualize the surface density of TMA⁺ ions adsorbed on the nanosheets, the area occupied by a single TMA⁺ ion is calculated based on each 2D rectangular lattice size and the replacement rate of exchangeable protons (see the Supporting Information). Figure 6 illustrates schematic models of adsorbed TMA⁺ ions on the host layer of the Ti_{1.73}O₄^{1.08-} swollen crystal in comparison with those on the surfaces of deionized nanosheets.^{30,39} For all of the deionized nanosheets, the occupied area exceeds the projected size of a TMA⁺ ion situated in a typical orientation,³⁷ allowing gaps between them. As shown in Figure 6a,b, a comparison between the deionized nanosheet of Ti_{1.73}O₄^{1.08-} and the swollen crystal reveals that the density of TMA⁺ ions decreases following the deionization process. This result suggests that the repeated deionization process not only removes dissociated TMA⁺ ions in the suspension but also reduces the amount of adsorbed TMA⁺ ions, causing a decreased ratio to exchangeable protons.

Moreover, the packing density of TMA⁺ ions on the surface of deionized Ti₂NbO₇⁻ is nearly equivalent to that on the deionized Ti_{1.73}O₄^{1.08-} nanosheet (Figure 6b,d), whereas the density on the surface of the deionized TiNbO₅⁻ nanosheet apparently increases and appears comparable to that on the host layer of the Ti_{1.73}O₄^{1.08-} swollen crystal (Figure 6a,c). These results indicate that the area occupied by TMA⁺ under low-ionic-strength conditions varies, depending on the type of nanosheets. The variation in TMA⁺ adsorption can be related to its intrinsic structural charge characteristics. As indicated in Table 1, charge densities of the nanosheets were calculated based on the number of compensating cations required to neutralize the net negative charge per unit cell, which also reflects the available acidic sites. For Ti₂NbO₇⁻ and TiNbO₅⁻, the measured TMA⁺ amount increases with the surface charge increasing from 5.7 to 8.2 e nm⁻². Although steric hindrance may prevent the stoichiometric adsorption of TMA⁺ on every available site, the observed trend suggests a possible correlation between charge density and TMA⁺ uptake. On the other hand, Ti_{1.73}O₄^{1.08-} yields the lowest adsorption value despite the highest charge density (9.5 e nm⁻²). This discrepancy might be attributed to the peculiar lepidocrocite-type structure as shown in Figure S6, where Ti vacancies (2.37 sites/nm²) can act as preferential binding sites for cationic species.⁴⁰ In addition, it has been reported that protonic titanoniobates generally exhibit stronger Brønsted acidity than titanates, due to the incorporation of a higher valent central metal (Nb⁵⁺).^{41,42} Therefore, the adsorption behavior appears to be dictated by a combination of factors, including the solid acidity, charge density, and number of adsorption sites, as well as the steric compatibility. From Table 1, it seems that the quantity of dissociated TMA⁺ generally correlates with the amount adsorbed on the nanosheet surface, resulting in the highest ionic strength of the deionized suspension of TiNbO₅⁻.

The above analyses thus indicate that the intersheet spacing is mainly determined by ionic strength, i.e., the Debye screening length of the deionized suspension, which is directly related to the structure of the nanosheets. For example, the differences in charge and thickness could qualitatively explain why TiNbO₅⁻ exhibits a relatively smaller intersheet spacing than those of Ti₂NbO₇⁻ and Ti_{1.73}O₄^{1.08-}.

Previous results have demonstrated that structural colors in nanosheet suspensions responded sensitively to changes in the chemical environment, such as pH-responsive behavior reported for Ti_{1.73}O₄^{1.08-}.¹² As shown in Figure S7, the pH responses of TiNbO₅⁻ and Ti₂NbO₇⁻ suspensions were evaluated. For the Ti₂NbO₇⁻ suspension, as pH approached neutrality, the reflection peak shifted toward a shorter wavelength (blue shift), and the reflection intensity gradually decreased. This suggests that the protonation of the nanosheet surface and the partial desorption of TMA⁺ accompanying the neutralization of the suspension induced a decrease in electrostatic repulsion between nanosheets, resulting in a reduction in the intersheet spacing and a decrease in the orientation order. On the other hand, a similar decrease in reflection intensity was observed for the TiNbO₅⁻ suspension, but the change in the reflection peak wavelength was not very evident. This behavior implies that the electrostatic repulsion between nanosheets was largely maintained without any significant reduction in intersheet spacing. The decrease in reflection intensity may be due to increasing orientational disorder of the nanosheets, but the exact cause remains to be explored. Nevertheless, the above results indicate that the pH-responsive behavior is dependent on the type and surface characteristics of the nanosheets, which may be useful for a tailored design of optical sensors.

A comparison summarizing the structural coloration behavior of representative 2D materials is shown in Table S2. Among them, transition metal oxide nanosheets exhibit a notably wide reflection wavelength range and high reflectance, demonstrating their potential as high-performance structural color materials. In addition to the nontoxic nature, the high refractive index and low background absorption of transition metal oxide nanosheets are beneficial in the realization of high reflection intensity and clear color tones. The high surface charges also enable dispersion stability without aggregation across a wide concentration range, generating highly tunable intersheet spacing and the resultant structural colors. The quantitative evaluation and comparative study of multiple metal oxide nanosheets presented in this study provide valuable insights, as well as general guidelines for the rational control of structural colors based on various 2D materials with different compositions and structures.

CONCLUSIONS

A comparative study on structural colors obtained from three types of transition metal oxide nanosheets was conducted. It was found that the nature of the structural colors is dependent on the structure of the nanosheets and the ionic strength of the resulting suspension. In general, larger ionic strength results in smaller intersheet spacing due to the effective shielding of electrostatic repulsive forces, leading to a blue shift of the structural color or even the disappearance of the visible structural color. Upon repeating the deionization process of the nanosheet suspensions, the ionic strength is diminished with the decreased concentrations of TMA⁺ and hydroxide ions. The concentration of dissociated ions as well as the

amount of TMA⁺ adsorbed on the nanosheet surface are strongly correlated with the charge feature of the nanosheets. This could well explain the result that TiNbO₅[−] nanosheets exhibit the smallest intersheet spacing in comparison with Ti₂NbO₇[−] and Ti_{1.73}O₄^{1.08−}. Moreover, when sufficient electrostatic repulsion is attained at the same volume fraction of nanosheets with different thicknesses, a larger intersheet spacing and the corresponding longer wavelength of structural color were yielded for thicker nanosheets, such as Ti₂NbO₇[−]. While previous studies have focused on a single type of nanosheet, the current study covers multiple metal oxide nanosheets with different compositions to verify the mechanism of structural color formation. The comparative exploration of plausible models and the measured values (such as TMA⁺ adsorption, exchangeable proton quantity, and ζ-potential) greatly deepens the understanding of the macroscopic ordering and/or liquid crystallinity of nanosheet suspensions.

Structural coloration of colloidal nanosheets is not only promising in chromic technology highly sensitive to even small environmental changes, but it is also attractive in exploring multifunctions derived from 2D materials. Transition metal oxide nanosheets are known for versatile properties, such as high UV absorption, photocatalytic activity, and a superior dielectric constant. The important insights revealed in the current study may help accelerate the research on fabricating mechano-thermo-photochromic devices based on colloidal nanosheets.

EXPERIMENTAL SECTION

Preparation of Titanoniobates and Titanate Nanosheet Dispersions

The nanosheet suspensions were synthesized according to procedures reported previously.^{3,43–45} Layered metal oxide polycrystals of KTiNbO₅, CsTi₂NbO₇, and K_{0.8}Ti_{1.73}Li_{0.27}O₄ were synthesized via a solid-state reaction. These polycrystals were proton-exchanged to form HTiNbO₅, HTi₂NbO₇·2H₂O, and H_{1.08}Ti_{1.73}O₄·H₂O by the treatment with HCl and then delaminated by vigorously shaking with an aqueous TMAOH solution (TMA⁺/H⁺ = 1.0). The resulting suspensions were subjected to centrifugation at an appropriate speed to remove the unexfoliated materials. The nanosheet suspension was diluted and dropped onto a clean silicon substrate. After drying, AFM observation was carried out to characterize the thickness and lateral size of the nanosheets. The volume fractions of the nanosheets were calculated from their molar concentration, as reported in the literature.¹¹ The molar concentrations were determined by gravimetric analysis of the powder that remained after drying the nanosheet suspension, followed by heating at 1000 °C.

Deionization Process and Structural Color Measurement

As previously reported,¹² excessive ions in the suspension were removed by the following deionization procedure. The centrifuge tube containing 25 cm³ of nanosheet dispersion was centrifuged (15 000 rpm, 1 h), settling out all dispersed nanosheets in the suspension. The supernatant was removed using a pipette. The same volume of pure water was added, and the sediment was redispersed by stirring with a vortex mixer. This operation was typically repeated 15 times for titanate nanosheets and 10 times for the other two titanoniobates until the ionic conductivity was below 0.01 mS cm^{−1}, which is comparable to that of a 0.1 mM TMAOH aqueous solution. The deionized suspension was injected into a homemade thin quartz glass cell with a gap of 0.13 mm (see Figure S4). The reflectance spectra of the suspensions sealed in the cells were measured with a UV–vis spectrophotometer. A standard white reflector was used as a baseline for the measurements, and a spectrum from the same cell filled with pure water was used to cancel the absorption by the solvent.

Characterization of Deionization Process in Nanosheet Dispersion

A change in the concentration of each ion in the suspension during the deionization process was monitored by pH, ion conductivity, and ¹H NMR measurements. The hydroxide ions in the suspension were determined by pH measurement. As the nanosheet suspension contains mainly TMA⁺ and hydroxide ions as free ions, the concentration of dissociated TMA⁺ was calculated by using the ion conductivity data as well as the amount of hydroxide ions obtained from the pH measurement. ¹H NMR was used to quantify the concentration of TMA⁺ in the suspension by comparing the area of the peak of TMA⁺ and DMSO added as an internal standard. This value is the sum of dissociated and adsorbed TMA⁺, and the concentration of TMA⁺ adsorbed on the nanosheets was calculated by subtracting the concentration of free ions. The ζ-potential of the deionized nanosheet suspension was measured by electrophoretic light scattering, and the average value obtained from at least five measurements was used as the ζ-potential. The concentration was unified at 0.04 vol % by diluting the original nanosheet suspension with pure water. To evaluate the pH-responsive behavior, a diluted hydrochloric acid solution (20 μM for Ti₂NbO₇[−] or 200 μM for TiNbO₅[−]) was added dropwise to the deionized suspensions. The changes in the reflection spectrum were monitored.

ASSOCIATED CONTENT

Supporting Information

The Supporting Information is available free of charge at <https://pubs.acs.org/doi/10.1021/jacsau.5c01152>.

Material characterizations, additional AFM images and lateral size histograms, structural color observation, estimation of the area occupied by TMA⁺ ions on the nanosheet surface, estimation of the exchangeable proton content in layered protonic oxides, cross-sectional schematic illustrations of the nanosheet structures, pH responses of structural colors, and comparison of the structural colors of 2D materials (PDF)

AUTHOR INFORMATION

Corresponding Authors

Takayoshi Sasaki – Research Center for Materials Nanoarchitectonics (MANA), National Institute for Materials Science (NIMS), Tsukuba, Ibaraki 305-0044, Japan; orcid.org/0000-0002-2872-0427; Email: SASAKI.Takayoshi@nims.go.jp

Renzhi Ma – Research Center for Materials Nanoarchitectonics (MANA), National Institute for Materials Science (NIMS), Tsukuba, Ibaraki 305-0044, Japan; Graduate School of Advanced Science and Engineering, Waseda University, Shinjuku-ku, Tokyo 169-8555, Japan; orcid.org/0000-0001-7126-2006; Email: MA.Renzhi@nims.go.jp

Authors

Takayuki Kikuchi – Research Center for Materials Nanoarchitectonics (MANA), National Institute for Materials Science (NIMS), Tsukuba, Ibaraki 305-0044, Japan; Graduate School of Advanced Science and Engineering, Waseda University, Shinjuku-ku, Tokyo 169-8555, Japan; orcid.org/0000-0003-0588-2172

Yasuo Ebina – Research Center for Materials Nanoarchitectonics (MANA), National Institute for

Materials Science (NIMS), Tsukuba, Ibaraki 305-0044, Japan; orcid.org/0000-0003-3471-9825

Nobuyuki Sakai – Research Center for Materials Nanoarchitectonics (MANA), National Institute for Materials Science (NIMS), Tsukuba, Ibaraki 305-0044, Japan; orcid.org/0000-0002-9395-6751

Yoshiyuki Sugahara – Graduate School of Advanced Science and Engineering, Waseda University, Shinjuku-ku, Tokyo 169-8555, Japan; Kagami Memorial Research Institute for Materials Science and Technology, Waseda University, Shinjuku-ku, Tokyo 169-0051, Japan; orcid.org/0000-0003-2973-8052

Complete contact information is available at:
<https://pubs.acs.org/10.1021/jacsau.5c01152>

Notes

The authors declare no competing financial interest.

ACKNOWLEDGMENTS

This work was supported by the World Premier International Research Center Initiative (WPI), Ministry of Education, Culture, Sports, Science and Technology (MEXT), Japan, and CREST of the Japan Science and Technology Agency (JST) (grant nos. JPMJCR17N1 and JPMJCR22B1), Japan. R.M. acknowledges support from JSPS KAKENHI (22H01916). The authors are grateful to Dr. Yasuhiro Ishida, Dr. Koki Sano, and Dr. Nobuyoshi Miyamoto for helpful discussions.

REFERENCES

- (1) Onsager, L. The Effects of Shape on the Interaction of Colloidal Particles. *Ann. N.Y. Acad. Sci.* **1949**, *51*, 627–659.
- (2) Sasaki, T.; Watanabe, M. Osmotic Swelling to Exfoliation. Exceptionally High Degrees of Hydration of a Layered Titanate. *J. Am. Chem. Soc.* **1998**, *120*, 4682–4689.
- (3) Sasaki, T.; Ebina, Y.; Kitami, Y.; Watanabe, M.; Oikawa, T. Two-Dimensional Diffraction of Molecular Nanosheet Crystallites of Titanium Oxide. *J. Phys. Chem. B* **2001**, *105*, 6116–6121.
- (4) Treacy, M. M. J.; Rice, S. B.; Jacobson, A. J.; Lewandowski, J. T. Electron Microscopy Study of Delamination in Dispersions of the Perovskite-Related Layered Phases $K[Ca_2Na_{n-3}Nb_nO_{3n+1}]$: Evidence for Single-Layer Formation. *Chem. Mater.* **1990**, *2*, 279–286.
- (5) Schaak, R. E.; Mallouk, T. E. Prying Apart Ruddlesden–Popper Phases: Exfoliation into Sheets and Nanotubes for Assembly of Perovskite Thin Films. *Chem. Mater.* **2000**, *12*, 3427–3434.
- (6) Du, G. H.; Yu, Y.; Chen, Q.; Wang, R. H.; Zhou, W.; Peng, L. M. Exfoliating $KTiNbO_5$ Particles into Nanosheets. *Chem. Phys. Lett.* **2003**, *377*, 445–448.
- (7) Takagaki, A.; Sugisawa, M.; Lu, D.; Kondo, J. N.; Hara, M.; Domen, K.; Hayashi, S. Exfoliated Nanosheets as a New Strong Solid Acid Catalyst. *J. Am. Chem. Soc.* **2003**, *125*, 5479–5485.
- (8) Fang, M. M.; Kim, C. H.; Saupe, G. B.; Kim, H. N.; Waraksa, C. C.; Miwa, T.; Fujishima, A.; Mallouk, T. E. Layer-by-Layer Growth and Condensation Reactions of Niobate and Titanoniobate Thin Films. *Chem. Mater.* **1999**, *11*, 1526–1532.
- (9) Miyamoto, N.; Nakato, T. Liquid Crystalline Nature of $K_4Nb_6O_{17}$ Nanosheet Sols and Their Macroscopic Alignment. *Adv. Mater.* **2002**, *14*, 1267–1270.
- (10) Nakato, T.; Miyamoto, N.; Harada, A. Stable Liquid Crystalline Phases of Colloidally Dispersed Exfoliated Layered Niobates. *Chem. Commun.* **2004**, 78–79.
- (11) Nakato, T.; Yamashita, Y.; Kuroda, K. Mesophase of Colloidally Dispersed Nanosheets Prepared by Exfoliation of Layered Titanate and Niobate. *Thin Solid Films* **2006**, *495*, 24–28.
- (12) Sano, K.; Kim, Y. S.; Ishida, Y.; Ebina, Y.; Sasaki, T.; Hikima, T.; Aida, T. Photonic Water Dynamically Responsive to External Stimuli. *Nat. Commun.* **2016**, *7*, No. 12559.
- (13) Shen, T.-Z.; Hong, S.-H.; Lee, B.; Song, J.-K. Bottom-Up and Top-Down Manipulations for Multi-Order Photonic Crystallinity in a Graphene-Oxide Colloid. *NPG Asia Mater.* **2016**, *8*, No. e296.
- (14) Li, P.; Wong, M.; Zhang, X.; Yao, H.; Ishige, R.; Takahara, A.; Miyamoto, M.; Nishimura, R.; Sue, H.-J. Tunable Lyotropic Photonic Liquid Crystal Based on Graphene Oxide. *ACS Photonics* **2014**, *1*, 79–86.
- (15) Gabriel, J.-C. P.; Camerel, F.; Lemaire, B. J.; Desvieux, H.; Davidson, P.; Batail, P. Swollen Liquid-Crystalline Lamellar Phase Based on Extended Solid-like Sheets. *Nature* **2001**, *413*, 504–508.
- (16) El Rifaii, K.; Wensink, H. H.; Goldmann, C.; Michot, L.; Gabriel, J.-C. P.; Davidson, P. Fine Tuning the Structural Colours of Photonic Nanosheet Suspensions by Polymer Doping. *Soft Matter* **2021**, *17*, 9280–9292.
- (17) Wong, M.; Ishige, R.; Hoshino, T.; Hawkins, S.; Li, P.; Takahara, A.; Sue, H.-J. Solution Processable Iridescent Self-Assembled Nanoplatelets with Finely Tunable Interlayer Distances Using Charge- and Sterically Stabilizing Oligomeric Polyoxalkylene-amine Surfactants. *Chem. Mater.* **2014**, *26*, 1528–1537.
- (18) Zeng, M.; King, D.; Huang, D.; Do, C.; Wang, L.; Chen, M.; Lei, S.; Lin, P.; Chen, Y.; Cheng, Z. Iridescence in Nematics: Photonic Liquid Crystals of Nanoplates in Absence of Long-Range Periodicity. *Proc. Natl. Acad. Sci. U.S.A.* **2019**, *116*, 18322–18327.
- (19) Masud, A. R.; Hong, S.-H.; Shen, T.-Z.; Shahzad, A.; Song, J.-K. Electrically and Electrohydrodynamically Driven Phase Transition and Structural Color Switching of Oligomer Tethered 2D Colloid. *RSC Adv.* **2018**, *8*, 16549–16556.
- (20) Mouri, E.; Fukumoto, T.; Kato, R.; Miyamoto, N.; Nakato, T. Time Evolution of the Inner Structure of Antimony Phosphate Nanosheet Suspension Developing Structural Colouration. *Soft Matter* **2024**, *20*, 6353–6360.
- (21) Mouri, E.; Ogami, C.; Fukumoto, T.; Nakato, T. Development of Structural Color by Niobate Nanosheet Colloids. *Chem. Lett.* **2020**, *49*, 717–720.
- (22) Miyamoto, N.; Yamamoto, S. Angular-Independent Structural Colors of Clay Dispersions. *ACS Omega* **2022**, *7*, 6070–6074.
- (23) Michels-Brito, P. H.; Dudko, V.; Wagner, D.; Markus, P.; Papastavrou, G.; Michels, L.; Breu, J.; Fossum, J. O. Bright, Noniridescent Structural Coloration from Clay Mineral Nanosheet Suspensions. *Sci. Adv.* **2022**, *8*, No. eab18147.
- (24) Yang, W.; Yamamoto, S.; Sueyoshi, K.; Inadomi, T.; Kato, R.; Miyamoto, N. Perovskite Nanosheet Hydrogels with Mechanochromic Structural Color. *Angew. Chem., Int. Ed.* **2021**, *60*, 8466–8471.
- (25) Shen, T.-Z.; Perera, K. N. A.; Masud, A. R.; Priyadarshana, P. A. N. S.; Park, J.-Y.; Wang, Q.-H.; Hong, S.-H.; Song, J.-K. A Dual-Frequency Photonic Crystal Nanocolloid with Hue- and Brightness-Tunable Structural Colors. *Cell Rep. Phys. Sci.* **2023**, *4*, No. 101343.
- (26) Szendrei, K.; Ganter, P.; Sánchez-Sobrado, O.; Eger, R.; Kuhn, A.; Lotsch, B. V. Touchless Optical Finger Motion Tracking Based on 2D Nanosheets with Giant Moisture Responsiveness. *Adv. Mater.* **2015**, *27*, 6341–6348.
- (27) Ganter, P.; Szendrei, K.; Lotsch, B. V. Towards the Nanosheet-Based Photonic Nose: Vapor Recognition and Trace Water Sensing with Antimony Phosphate Thin Film Devices. *Adv. Mater.* **2016**, *28*, 7436–7442.
- (28) Gong, T.; Zhang, X.; Fu, Y.; Zhou, G.; Chi, H.; Li, T. A Facile Fabrication of Colorimetric Graphene Oxide Reflecting Films for Ultrasensitive Optical Gas Sensing. *Sens. Actuators, B* **2018**, *261*, 83–90.
- (29) Lotsch, B. V.; Ozin, G. A. Clay Bragg Stack Optical Sensors. *Adv. Mater.* **2008**, *20*, 4079–4084.
- (30) Akatsuka, K.; Takanashi, G.; Ebina, Y.; Haga, M.; Sasaki, T. Electronic Band Structure of Exfoliated Titanium- and/or Niobium-Based Oxide Nanosheets Probed by Electrochemical and Photoelectrochemical Measurements. *J. Phys. Chem. C* **2012**, *116*, 12426–12433.

- (31) Yamaguchi, D.; Miyamoto, N.; Fujita, T.; Nakato, T.; Koizumi, S.; Ohta, N.; Yagi, N.; Hashimoto, T. Aspect Ratio Dependent Phase Transitions and Concentration Fluctuations in Aqueous Colloidal Dispersions of Charged Plate-Like Particles. *Phys. Rev. E* **2012**, *85*, No. 011403.
- (32) Deggelmann, M.; Palberg, T.; Hagenbüchle, M.; Maier, E. E.; Krause, R.; Graf, C.; Weber, R. Electrokinetic Properties of Aqueous Suspensions of Polystyrene Spheres in the Gas and Liquid-like Phase. *J. Colloid Interface Sci.* **1991**, *143*, 318–326.
- (33) Robinson, R. A.; Stokes, R. H. *Electrolyte Solutions*; Courier Corporation, 2002.
- (34) Miyamoto, N.; Nakato, T. Liquid Crystalline Inorganic Nanosheet Colloids Derived from Layered Materials. *Isr. J. Chem.* **2012**, *52*, 881–894.
- (35) Smalley, M. V. *Clay Swelling and Colloid Stability*, 1st ed.; CRC Press: Boca Raton, FL, 2006.
- (36) Takagaki, A.; Yoshida, T.; Lu, D.; Kondo, J. N.; Hara, M.; Domen, K.; Hayashi, S. Titanium Niobate and Titanium Tantalate Nanosheets as Strong Solid Acid Catalysts. *J. Phys. Chem. B* **2004**, *108*, 11549–11555.
- (37) Song, Y.; Sakai, N.; Ebina, Y.; Iyi, N.; Kikuchi, T.; Ma, R.; Ishida, Y.; Sasaki, T. Systematic Study on Swelling/Delamination of Layered Metal Oxides with Quaternary Ammonium Ions: Production of Well-Shaped/Oversized Unilamellar Nanosheets. *Small Methods* **2025**, *9*, No. 2401055.
- (38) Momma, K.; Izumi, F. VESTA 3 for Three-dimensional Visualization of Crystal, Volumetric and Morphology Data. *J. Appl. Crystallogr.* **2011**, *44*, 1272–1276.
- (39) Sakai, N.; Suzuki, M.; Sasaki, T. Scission of 2D Inorganic Nanosheets via Physical Adsorption on a Nonflat Surface. *Adv. Mater. Interfaces* **2022**, *9*, No. 2102591.
- (40) Sonotani, A.; Shimada, T.; Takagi, S. “Size-Matching Effect” in a Cationic Porphyrin–Titania Nanosheet Complex. *Chem. Lett.* **2017**, *46*, 499–501.
- (41) Sasaki, T.; Izumi, F.; Watanabe, M. Intercalation of Pyridine in Layered Titanates. *Chem. Mater.* **1996**, *8*, 777–782.
- (42) Jacobson, A. J.; Johnson, J. W.; Lewandowski, J. T. Intercalation of the Layered Solid Acid $\text{HCa}_2\text{Nb}_3\text{O}_{10}$ by Organic Amines. *Mat. Res. Bull.* **1987**, *22*, 45–51.
- (43) Shibata, T.; Takanashi, G.; Nakamura, T.; Fukuda, K.; Ebina, Y.; Sasaki, T. Titanoniobate and Niobate Nanosheet Photocatalysts: Superior Photoinduced Hydrophilicity and Enhanced Thermal Stability of Unilamellar Nb_3O_8 Nanosheet. *Energy Environ. Sci.* **2011**, *4*, 535–542.
- (44) Sasaki, T.; Watanabe, M.; Hashizume, H.; Yamada, H.; Nakazawa, H. Macromolecule-like Aspects for a Colloidal Suspension of an Exfoliated Titanate. Pairwise Association of Nanosheets and Dynamic Reassembling Process Initiated from It. *J. Am. Chem. Soc.* **1996**, *118*, 8329–8335.
- (45) Tanaka, T.; Ebina, Y.; Takada, K.; Kurashima, K.; Sasaki, T. Oversized Titania Nanosheet Crystallites Derived from Flux-grown Layered Titanate Single Crystals. *Chem. Mater.* **2003**, *15*, 3564–3568.



CAS INSIGHTS™

EXPLORE THE INNOVATIONS SHAPING TOMORROW

Discover the latest scientific research and trends with CAS Insights. Subscribe for email updates on new articles, reports, and webinars at the intersection of science and innovation.

Subscribe today

CAS
A division of the American Chemical Society